

Strong and Weak Deflection of Light in the Equatorial Plane of a Kerr Black Hole

S. V. Iyer* and E. C. Hansen†

*Department of Physics & Astronomy,
State University of New York at Geneseo,
1 College Circle, Geneseo, NY 14454.*

Abstract

Analytical series expansions for the bending of light in the equatorial plane of a Kerr black hole are presented in both the strong and weak deflection regimes. It is critical that these are known in analytical form so further analysis can be done for predicting different properties of images formed in gravitational lensing. Starting with the exact bending angle in terms of the spin parameter, we apply a perturbative scheme for rewriting the bending angle as series expansions in terms of the impact parameter of the incident light ray. The asymmetry introduced by the black hole spin results in spin-dependent shifts in image positions. We apply our results for the case of a galactic supermassive black hole to predict angular shifts of relativistic images from the optic axis. This would not be possible without the perturbative expansions in the strong deflection regime, only in which relativistic images have a chance of being resolved by future telescopes.

Keywords: gravitational lensing, bending angle, relativistic images, Kerr black hole

*Electronic address: iyer@geneseo.edu

†Electronic address: ech3@geneseo.edu

I. INTRODUCTION

Observations of the bending of light near the sun in the early twentieth century and Einstein rings in deep space Hubble space telescope images in the last decade or so are both examples of tests of general relativity in the weak field limit, or more precisely, the weak deflection limit. As the light ray skims by, not far from the horizon, however, a richer variety of lensing effects are predicted to occur, awaiting observation by telescopes with much higher viewing power than what is available today. Bending angle calculations [1, 2, 3, 4, 5] for Schwarzschild and Kerr geometries show that as we approach the depths of the gravitational potential, multiple looping of the light ray around the center of attraction is possible resulting in what are known as relativistic images (see for example, [6]). In the case of a Schwarzschild black hole, as the distance of closest approach r_0 nears the critical value of $3m_\bullet$, where $m_\bullet = GM/c^2$ is its gravitational radius, the bending angle has a logarithmic form. When expressed in terms of the invariant quantity $b' = 1 - b_c/b$, where $b_c = 3\sqrt{3}m_\bullet$, this strong deflection limit (SDL) of the bending angle is given by [7]

$$\hat{\alpha}(b') = -\pi + \log \left[\frac{216 (7 - 4\sqrt{3})}{b'} \right] + \mathcal{O}[b'] + \dots \quad (1)$$

This result is similar, but not identical, to the Darwin logarithmic term [1]; this result takes into account an improvement to Darwin's result close to the photon sphere. The detailed formulation that makes this modification to the strong deflection limit was recently published in [7].

In this paper, we show that the analysis can be applied to the spinning, or Kerr, black hole for the case when the light ray stays on the equatorial plane. In order to determine the perturbative series for the bending angle, an explicit expression in terms of just the spin and mass of the black hole as a function of the impact parameter is needed as the starting point. Such an expression was recently derived in [8]. The bending angle was expressed explicitly in terms of the black hole mass $m_\bullet = GM/c^2$ and the black hole spin parameter $a = J/Mc$, where J/M is the angular momentum per unit mass of the black hole. With a new definition for b' that includes the non-zero spin of the black hole, we define precisely the approach to the critical impact parameter, and thus the strong deflection limit (SDL).

The weak deflection limit (WDL), on the other hand, in both the Schwarzschild and the Kerr case are easily defined in terms of the impact parameter as the limit $b \rightarrow \infty$. In this

limit, the weak deflection bending angle series for the Schwarzschild case is given by

$$\hat{\alpha}(b) = 4 \left(\frac{m_\bullet}{b} \right) + \frac{15\pi}{4} \left(\frac{m_\bullet}{b} \right)^2 + \mathcal{O} \left[\left(\frac{m_\bullet}{b} \right)^3 \right] + \dots \quad (2)$$

A partial generalization of this result for the Kerr case in terms of the coordinate-dependent variable r_0 was obtained by Boyer-Lindquist, Skrotskii, Plebanski [10, 11, 12] and from a numerical treatment by Rauch and Blandford [9]. The Kerr WDL series in terms of the impact parameter was recently obtained in a completely different context by Petters [13].

In this paper, we continue to work in the same perturbative framework that was started in [7] and apply it to the case of deflection of rays confined to the Kerr equatorial plane. Bending angles, and therefore the position and magnification of images, depend crucially on whether the light ray is traversing in the same or opposite direction to the rotation. For this reason, throughout the analysis, we carefully keep track of whether the ray orbits are direct or retrograde. The perturbative corrections are obtained in a manner very similar to that for the Schwarzschild case presented in [7].

The need for analytical results for the bending angle cannot be overemphasized given that important lensing variables like image positions, magnifications and time delays depend crucially on these results. See [14]-[18] for many different approaches towards analytical results. Perturbative analysis is extremely useful in order to verify, at least to leading orders, the predictions of strong deflection lensing. Specific to the Kerr case, we also need to be able to glean the contribution to light deflection arising purely from spin. Furthermore, higher order relativistic images can be analyzed only in the strong deflection regime, making this an important approach to test general relativity beyond the usual classical tests in the weak field regime.

In Section 2, we start with the bending angle result from [8] and definitions of some of the variables to be used in the series expansions. We present the weak and strong deflection series expansion terms in Sections 3 and 4 respectively, along with numerical plot comparisons of these terms with the exact result.

As a quick preview, we present here two plots that illustrate the main focus of this paper: the 2nd-order strong deflection and the 6th-order weak deflection bending angles are plotted alongside the exact bending angle for comparison, for direct and retrograde orbits in Figures 1 and 2 showing that our series expansions have excellent accuracy; the SDL series and WDL series apply nicely in the two regimes. Note that the two assumptions we have made here

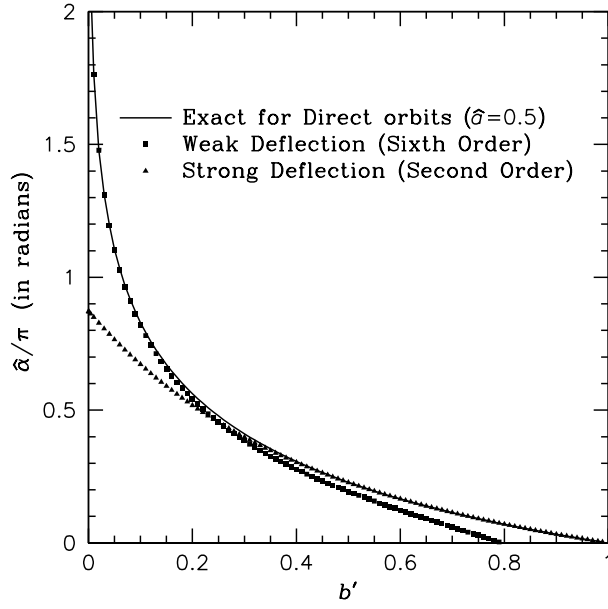


FIG. 1: The 2nd-order strong deflection and the 6th-order weak deflection are plotted alongside the numerically integrated exact formal Kerr bending angle $\hat{\alpha}$ (in units of π) for direct orbits.

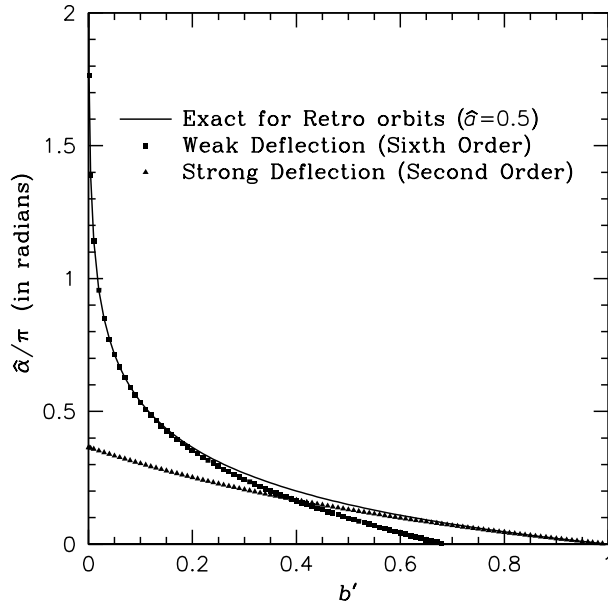


FIG. 2: The 2nd-order strong deflection and the 6th-order weak deflection are plotted alongside the numerically integrated exact formal Kerr bending angle $\hat{\alpha}$ (in units of π) for retro orbits.

are: (1) the light ray stays on the equatorial plane, and (2) the spin parameter stays in the range $0 \leq a < m_\bullet$. As can be seen in the plots, the agreement between the exact and our series expansions is better in the direct than in the retro case.

In section 5 is presented an application of both series to the simplest case of lensing geometry in which the source, lens and the observer are in perfect alignment. We show that the usual calculation for the Einstein angle that uses the WDL bending angle is applicable in the Kerr case as well. However, since there is no contribution to first order, the Einstein ring radius and angle are indistinguishable from the static case. In the strong deflection limit, on the other hand, the effect of spin on the angular positions relativistic images is relatively much greater. This numerical calculation is analogous to the one for the Schwarzschild case found in Virbhadra and Ellis [19]. We show that the shift in the image position increases with the black hole angular momentum.

II. FORMAL EXACT BENDING ANGLE FOR THE EQUATORIAL KERR CASE

Let us now consider a light ray that starts in the asymptotic region and approaches the black hole, with r_0 as the distance of closest approach. It then emerges and reaches an observer who is also in an asymptotic region.

We will use the following convenient notation:

$$h = \frac{m_\bullet}{r_0} \quad \omega_s = \frac{a}{b_s} \quad \text{and} \quad \omega_0 = \frac{a^2}{m_\bullet^2} \quad (3)$$

where $b_s = sb$ is the invariant impact parameter. The parameter s will be used to keep track of the sign of the impact parameter relative to the black hole spin. : $s = +1$ for direct orbits and $s = -1$ for retrograde orbits. Quantities that have s as subscript obey the same sign convention. For example, ω_s takes on the appropriate sign for direct and retrograde orbit. Note that in the limit $\{\omega_s, \omega_0 \rightarrow 0\}$, we recover the zero-spin Schwarzschild case, and in the limit $h \rightarrow 0$, we have the zero-deflection flat metric limit. With $a = J/Mc$ it is also convenient to introduce

$$\hat{a} = \frac{a}{m_\bullet} = \frac{Jc}{GM^2}, \quad (4)$$

as the “normalized” spin parameter. We will limit ourselves to cases where $0 \leq \hat{a} \leq 1$, with $\hat{a} = 0$ being the Schwarzschild limit and $\hat{a} = 1$ being extreme Kerr. Next, we define critical

parameters analogous to the Schwarzschild case in [7]:

$$h_{sc} = \frac{1 + \omega_s}{1 - \omega_s} \quad \text{and} \quad r_{sc} = \frac{3m_\bullet}{h_{sc}} \quad (5)$$

We also define the variable

$$h' = 1 - \frac{3h}{h_{sc}} \equiv 1 - 3 \left(\frac{m_\bullet}{r_0} \right) \left(\frac{1 - \omega_s}{1 + \omega_s} \right) \quad (6)$$

with

$$1 - 3 \left(\frac{m_\bullet}{r_0} \right) \left(\frac{1 - \omega_s}{1 + \omega_s} \right) \xrightarrow{a \rightarrow 0} 1 - \frac{3m_\bullet}{r_0}.$$

We have introduced these different quantities for the Kerr case, keeping in mind that they should go over to those defined in the Schwarzschild case smoothly when a is set equal to zero. So, as shown above, as $a \rightarrow 0$, $h_{sc} \rightarrow 1$ and we recover the definition of h' in [7]. In both cases, $h \rightarrow 0$ at critical, and $h \rightarrow 1$ as r_0 approaches infinity.

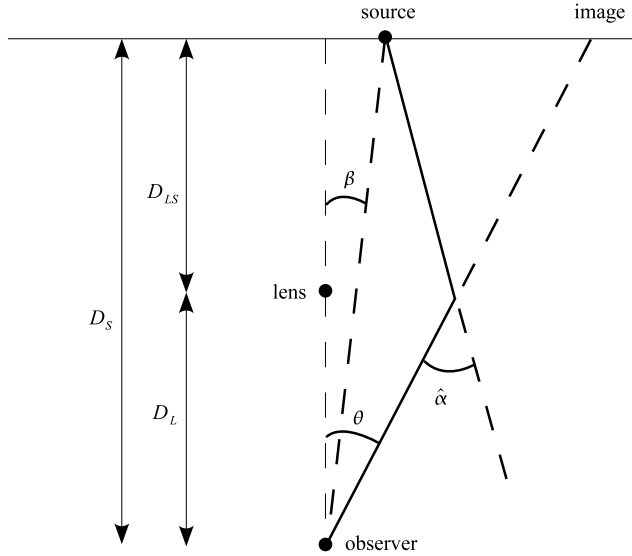


FIG. 3: *Thin lens geometry.*

Critical values for the radius and the impact parameters in Kerr geometry are given by:

$$r_{sc} = 3m_\bullet \frac{\left(1 - \frac{a}{b_{sc}}\right)}{\left(1 + \frac{a}{b_{sc}}\right)} \quad (7)$$

and

$$(b_{sc} + a)^3 = 27m_\bullet^2(b_{sc} - a). \quad (8)$$

From a lensing perspective, we are interested in impact parameters just beyond the critical value (SDL) extending all the way to infinity (WDL). We define the dimensionless quantity b' as

$$b' = 1 - \frac{sb_{sc}}{b} \quad (9)$$

where the insertion of the quantity s guarantees that the b' stays between 0 and 1. Note that this definition goes over naturally in the Schwarzschild limit:

$$1 - \frac{sb_{sc}}{b} \xrightarrow{a \rightarrow 0} 1 - \frac{3\sqrt{3}m_{\bullet}}{b}$$

As will become apparent in later sections, the “normalized” impact parameter b' is extremely convenient and natural for describing the range of values from critical all the way to infinity.

The lensing geometry is shown in Figure 3 where it is assumed as usual that the thickness of the lens plane is much smaller than the distances between source and lens D_{LS} . The distance (from the observer) to the lens and source are denoted by D_L and D_S respectively. The angular position of the source, β and the image, θ are also shown in the figure.

The deflection of the light ray from its original path $\hat{\alpha}$ is given by the following expression[8].

$$\hat{\alpha} = -\pi + \frac{4}{1 - \omega_s} \sqrt{\frac{r_0}{Q}} \left\{ \Omega_+ [\Pi(n_+, k) - \Pi(n_+, \psi, k)] + \Omega_- [\Pi(n_-, k) - \Pi(n_-, \psi, k)] \right\}, \quad (10)$$

where $\Pi(n_{\pm}, k)$ and $\Pi(n_{\pm}, \psi, k)$ are the complete and the incomplete elliptic integrals of the third kind respectively. The argument k^2 is defined through the elliptic integral as usual in the range $0 \leq k^2 \leq 1$. Note that in some references the variable is referred to as k^2 and in others simply as k . The order in which the arguments appear in $\Pi(n, \psi, k)$ also varies between different references and in Mathematica.

Remark: In Mathematica, the built-in mathematical function for the incomplete elliptic integral of the third kind $\text{EllipticPi}[n, \phi, m]$ is defined by

$$\int_0^{\phi} [1 - n \sin^2 \theta]^{-1} [1 - m \sin^2 \theta]^{-1/2} d\theta$$

and the complete elliptic integral of the third kind is $\text{EllipticPi}[n, m] = \text{EllipticPi}[n, \pi/2, m]$.

In the limiting case when $a \rightarrow 0$, we have $\Omega_+ = 1$, $\Omega_- = 0$ and $n_+ = 0$ we have the

Schwarzschild result

$$\begin{aligned}\hat{\alpha} &= -\pi + 4\sqrt{\frac{r_0}{Q}} [\Pi(0, k) - \Pi(\psi, 0, k)] \\ &= -\pi + 4\sqrt{\frac{r_0}{Q}} [K(k) - F(\psi, k)],\end{aligned}\quad (11)$$

where $K(k)$ and $F(\psi, k)$ are the complete and incomplete integrals of the first kind respectively. In addition, in the limit when $\mathbf{m}_\bullet = 0$ (i.e., $h \rightarrow 0$) we recover zero deflection as expected.

The different variables are defined as follows:

$$\frac{r_0}{Q} = \frac{1}{h_{sc} \sqrt{\left(1 - \frac{2h}{h_{sc}}\right) \left(1 + \frac{6h}{h_{sc}}\right)}} \quad (12)$$

$$k^2 = \frac{\sqrt{\left(1 - \frac{2h}{h_{sc}}\right) \left(1 + \frac{6h}{h_{sc}}\right) + \frac{6h}{h_{sc}} - 1}}{2\sqrt{\left(1 - \frac{2h}{h_{sc}}\right) \left(1 + \frac{6h}{h_{sc}}\right)}} \quad (13)$$

$$\psi = \arcsin \frac{\sqrt{1 - \frac{2h}{h_{sc}} - \sqrt{\left(1 - \frac{2h}{h_{sc}}\right) \left(1 + \frac{6h}{h_{sc}}\right)}}}{\sqrt{1 - \frac{6h}{h_{sc}} - \sqrt{\left(1 - \frac{2h}{h_{sc}}\right) \left(1 + \frac{6h}{h_{sc}}\right)}}} \quad (14)$$

$$\Omega_\pm = \frac{\pm(1 \pm \sqrt{1 - \omega_0})(1 - \omega_s) \mp \omega_0/2}{\sqrt{1 - \omega_0} \left(1 \pm \sqrt{1 - \omega_0} - \frac{\omega_0 h_{sc}}{4} \left[1 - \frac{2h}{h_{sc}} - \sqrt{\left(1 - \frac{2h}{h_{sc}}\right) \left(1 + \frac{6h}{h_{sc}}\right)}\right]\right)} \quad (15)$$

$$n_\pm = \frac{1 - \frac{6h}{h_{sc}} - \sqrt{\left(1 - \frac{2h}{h_{sc}}\right) \left(1 + \frac{6h}{h_{sc}}\right)}}{1 - \frac{2h}{h_{sc}} - \sqrt{\left(1 - \frac{2h}{h_{sc}}\right) \left(1 + \frac{6h}{h_{sc}}\right)} - \frac{4}{\omega_0 h_{sc}} (1 \pm \sqrt{1 - \omega_0})} \quad (16)$$

We note here that the quantity b' appears in this expression via r_0, h, h_{sc} , and ω_s , while $\omega_0 = a^2/\mathbf{m}_\bullet^2$ is independent of the impact parameter. Any quantity that has an “s” in the subscript takes on a negative sign when on the retro side. The angle $\hat{\alpha}$ itself stays positive, i.e., the light ray is still deflected towards the axis of rotation albeit to a lesser extent on the

retro side [8]. In the next two sections, we outline the series expansions for the weak and strong deflection limits.

III. EXPANSION OF THE BENDING ANGLE BEYOND CRITICAL

As we did in [7], we show that the SDL bending angle can be expressed as an “affine perturbation” series in b' . The quantity b' is now defined appropriately for the equatorial Kerr case. The choice of variables turns out to be very important for carrying out the entire calculation successfully. Moreover, the series terms in the equatorial Kerr case become much lengthier because of the contribution from the non-zero spin.

We define an *affine perturbation* series about a function $g(x)$ as

$$f(x) = (A_0 + \cdots + A_p x^p + \cdots) g(x) + (B_0 + \cdots + B_q x^q + \cdots),$$

where A_i and B_i are constants with p and q positive rational numbers. Analogous to the Schwarzschild case, the the bending angle has an invariant affine perturbation series of the form

$$\hat{\alpha}(b') = \left(\sigma_0 + \sigma_1 (b') + \sigma_2 (b')^2 + \cdots \right) \log \left[\frac{\lambda_0}{b'} \right] \left(\rho_0 + \rho_1 (b') + \rho_2 (b')^2 + \cdots \right), \quad (17)$$

where λ_0 , σ_i and ρ_i are not just numerical constants, but also depend on the spin parameter a . Note that (17) is not a Taylor series expansion because of the appearance of the logarithmic term.

The formal expression (10) for the bending angle is just that; it is difficult to extract information about position and magnification of images as seen from the observer’s vantage point. The difference between the direct and retro orbits, for example, is simply not at all obvious if we just look at the formal exact expression. The effect of frame-dragging on the light ray is buried deep in the details of the expression. In what follows, we have sorted through these details being careful at each step to make sure that the Schwarzschild results are recovered whenever the spin parameter is turned off.

We begin by rewriting the expression in terms of the variables h , h_{sc} , ω_s , and ω_0 . The two regimes that we are referring to as SDL and WDL involve different series expansions of

elliptic integral of the third kind and these have to be carried out using the built-in EllipticPi functions and their properties in Mathematica. The WDL is easily expressed as the limit as $b \rightarrow 0$, while a precise definition of the SDL is a bit more involved. Following our scheme in [7], we introduce the variable $b' = 1 - sb_{sc}/b$ and consider the limit as $b' \rightarrow 0$. In this limit, we are approaching the critical impact parameter. Figure 4 is a schematic to show the limiting values of the different variables as the impact parameter goes from critical to infinity.

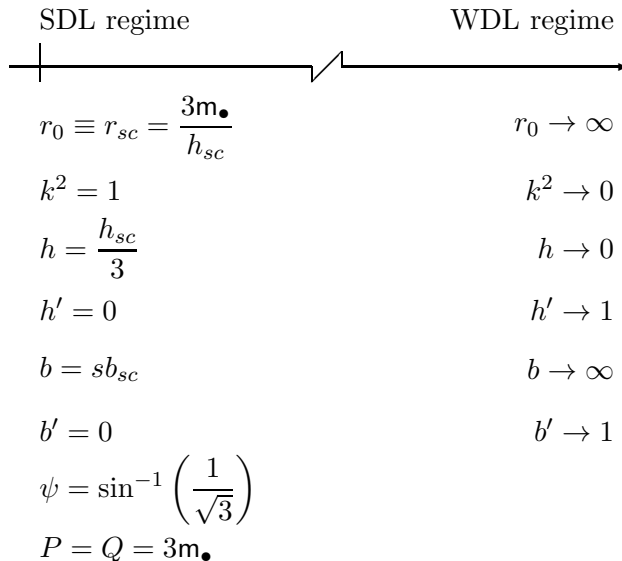


FIG. 4: A schematic to show the strong and weak deflection limits in terms of the relevant variables.

On the left hand side, we have all parameters and the corresponding limiting values as we approach critical radius. First, r_0 is defined in a similar way as we did in the Schwarzschild case [7]. The argument k^2 is defined through the elliptic integral as usual in the range $0 \leq k^2 \leq 1$. Note that in some references the variable is referred to as k^2 and in others, simply as k . The order in which the arguments appear in $\Pi(n, \psi, k)$ also varies between different references and in Mathematica. The variables h' and b' are both equivalent ways of describing the range of possible impact parameters. We will eliminate h' in the end to express all quantities in terms of b' in the end. The impact parameter b itself can be positive or negative and the sign is carried by s . Note that the impact parameter explicitly approaches critical on the left and infinity on the right. Some of the other intermediate variables are also given here for completeness. Once again, our goal is to express the bending angle in

terms of b' ; the only other quantities that will remain in our final results are \mathbf{m}_\bullet , \hat{a} and s . We have assumed that \hat{a} stays in the range $0 \leq \hat{a} < 1$. In addition to the variables shown in Figure 4, the argument n_\pm also stays in the range $\{0 \rightarrow 1\}$.

IV. WEAK DEFLECTION LIMIT

The weak deflection limit is simply defined by the limit as $b \rightarrow \infty$. Series expansions for the elliptic integrals are readily available in Mathematica. Before we present our result, we give here the existing correction to the Einstein bending angle that other authors have derived before. For example, the following result appeared in 1967 in one of the earliest papers on the Kerr metric by Boyer and Lindquist [10]:

$$\hat{\alpha} = 4 \frac{\mathbf{m}_\bullet}{r_0} \left(1 + \frac{a}{r_0} \right) \quad (18)$$

The r_0 is the Boyer-Lindquist “radial” coordinate or “the distance of closest approach”. This result is for direct orbits only and it clearly shows that there is no spin-dependent correction to the Einstein angle to first order in $1/b$. In the above result and in a number of other references, the direct orbit is one in which a is taken to be negative; this is a matter of convention. Similar results (some with the opposite sign convention) were also found by Skrotskii[11] and Plebanski[12] and others. Extensive numerical analysis can be found in Rauch and Blandford [9].

As in the Schwarzschild case, we have chosen to keep the expression in terms of the invariant quantity, b instead of r_0 . After a straightforward calculation and some simplification we obtain the following bending angle WDL series for the equatorial Kerr:

$$\begin{aligned} \hat{\alpha} = 4 \left(\frac{\mathbf{m}_\bullet}{b} \right) + \left[\frac{15\pi}{4} - 4s\hat{a} \right] \left(\frac{\mathbf{m}_\bullet}{b} \right)^2 + \left[\frac{128}{3} - 10\pi s\hat{a} + 4\hat{a}^2 \right] \left(\frac{\mathbf{m}_\bullet}{b} \right)^3 \\ + \left[\frac{3465\pi}{64} - 192s\hat{a} + \frac{285\pi}{16}\hat{a}^2 - 4s\hat{a}^3 \right] \left(\frac{\mathbf{m}_\bullet}{b} \right)^4 \quad (19) \end{aligned}$$

The spin parameter \hat{a} and the sign s appear explicitly in our series expansion. We will first note that the leading behavior of our result is in agreement with (18) after correcting for the sign; specifically, we do not see a correction to first order in $1/b$. As mentioned in the introduction, the leading terms of our series are in exact agreement with those obtained by Petters in a completely different context [13]. Note that some of the terms that depend

on the spin parameter are also sign sensitive. Although it may never be needed, the weak deflection series can be extended to include terms of much higher orders, for different values of \hat{a} and for both direct and retro orbits. As a first check of our result, we set $a = 0$ in equation (19)

$$\hat{\alpha}(b) = 4 \left(\frac{m_\bullet}{b}\right) + \frac{15\pi}{4} \left(\frac{m_\bullet}{b}\right)^2 + \frac{128}{3} \left(\frac{m_\bullet}{b}\right)^3 + \frac{3465\pi}{64} \left(\frac{m_\bullet}{b}\right)^4 + \mathcal{O} \left[\left(\frac{m_\bullet}{b}\right)^5\right] + \dots \quad (20)$$

and recover the Schwarzschild series [7].

In Figures 7-10 plot comparisons of the perturbative and exact Kerr bending angle are presented for $\hat{a} = 0.5$ and $\hat{a} = 0.99$ for both direct and retro orbits. Corrections up to first, second and third order in m_\bullet/b are plotted with the exact bending angle in each case. The plots clearly show that the weak deflection approximation gets closer to the exact angle as we include higher order terms. We have shown direct and retro plots to illustrate the effectiveness of the weak deflection series for both $s = +1$ and $s = -1$. We have chosen two representative values of \hat{a} for the plots; in fact, the series works nicely for all spins $0 \leq \hat{a} < 1$.

The correction to the Schwarzschild weak deflection bending angle coming from spin appears in second order ($1/b^2$) only. This means that the spin contribution would be nearly impossible to detect in the weak deflection regime. The Einstein ring, for example, when the source, lens and observer are perfectly aligned would be essentially the same for the Schwarzschild and Kerr case, making it extremely difficult to detect the spin contribution. As we will see shortly, the formation of relativistic images in the strong deflection limit is much more sensitive to the spin and for this reason would be a far more important tool for testing general relativity in the strong field limit and for studying the black hole spin itself.

V. STRONG DEFLECTION LIMIT

As we approach critical impact parameter, we once again see, as in the Schwarzschild case [7], that the leading behavior is logarithmic. In addition to this virulent term, the dependence on spin makes the series expansion quite complicated. We have nevertheless been able to extract the series terms up to second order in b' as defined in equation (17). The built-in series expansions in Mathematica have been used for this purpose[20]. Care must be taken with defining and providing the correct arguments for the Mathematica

functions and appropriate limits for the associated series. We give here only the zeroth order term for the bending angle:

$$\hat{\alpha}_{\text{SDL}}^{(0)} = -\pi + \frac{3\sqrt{\frac{1}{h_{sc}}} \left[2\sqrt{1-\omega_0} [3 - 2h_{sc}(1-\omega_s)] \log \left(\frac{12(2-\sqrt{3})}{h'} \right) + \sqrt{3} [U_- V_- + U_+ V_+] \right]}{\sqrt{1-\omega_0} [9 - h_{sc}(6 - h_{sc}\omega_0)] (1-\omega_s)}$$

where

$$U_{\pm} \equiv h_{sc} [\pm\omega_0 \mp 2(1-\omega_s) (1 \pm \sqrt{1-\omega_0})] \pm 3 [1 \pm \sqrt{1-\omega_0} - 2\omega_s]$$

$$V_{\pm} = \sqrt{\frac{h_{sc}\omega_0}{6 \pm 6\sqrt{1-\omega_0} + h_{sc}\omega_0}} \log \left[\frac{\left(1 + \sqrt{\frac{h_{sc}\omega_0}{6 \pm 6\sqrt{1-\omega_0} + h_{sc}\omega_0}} \right) \left(1 - \sqrt{\frac{3h_{sc}\omega_0}{6 \pm 6\sqrt{1-\omega_0} + h_{sc}\omega_0}} \right)}{\left(1 - \sqrt{\frac{h_{sc}\omega_0}{6 \pm 6\sqrt{1-\omega_0} + h_{sc}\omega_0}} \right) \left(1 + \sqrt{\frac{3h_{sc}\omega_0}{6 \pm 6\sqrt{1-\omega_0} + h_{sc}\omega_0}} \right)} \right]$$

We have written the bending angle in terms of h' because the full version explicitly in terms of b' is too complicated to show here. It can be shown, almost just by inspection of the above zeroth order term, that setting \hat{a} equal to zero (which means $\omega_s, \omega_0 \rightarrow 0$ and $h_{sc} \rightarrow 1$) yields the Schwarzschild version [7] immediately:

$$\hat{\alpha} = -\pi + 2 \log \left(\frac{12(2-\sqrt{3})}{h'} \right) + \mathcal{O}[h'] + \dots \quad (21)$$

In Figures 11-14 are shown plots of the strong deflection approximation and the exact bending angle. Due to the presence of both positive and negative terms in the series, the perturbative expression oscillates about the exact value and gets closer to the exact as we include more terms in the expansion.

VI. EINSTEIN RING AND PARA IMAGES

The weak and strong series expansions are applicable to either ends of the entire range of b' . When both the WDL and SDL series are taken together, they cover the entire range with accuracy. Figures 15 and 16 depict this for the case when $\hat{a} = 0.5$. The value of b' where the discrepancy plots criss-cross varies, depending on the spin value. In Figures 1 and

2, we showed plots of the 2nd-order strong series and the 6th-order weak series along with the exact for spin value of $\hat{a} = 0.5$. From all these plots it is clearly evident that our series expansion results are excellent approximations to the exact bending angle. This is essentially the same for all spin values between $0 \leq \hat{a} < 1$.

We present here an application of the strong deflection limit of the bending angle used along with the lens equation for the lens geometry shown in Figure 3 with the usual assumption that the thickness of the lens plane is negligible compared to the distances between the source, the lens and the observer. For the calculations shown here we will use the same model as in [19], where the mass of black hole is taken to be $2.8 \times 10^6 M_\odot$. With $D_{LS}/D_S = 1/2$ and $D_L = 8.5$ kpc, the angular radius of the Einstein ring can be calculated using $\theta_E = (4m_\bullet D_{LS}/D_L D_S)^{1/2}$. The Einstein ring is formed by a cone's worth of rays emanating from the source and symmetrically deflected by the black hole. In the Kerr case, we expect that the projection of these rays on the sky would still be a closed curve, except it won't have circular symmetry; depending on how the magnification varies, these could appear as arcs on the sky. Furthermore, our results apply only to light rays that stay on the equatorial plane, and hence the plane of incidence. Rays coming in at an angle to the equatorial plane, however, will not stay on the plane of incidence: the black hole spin will peel these away from the plane of incidence (see [18] and [17]). Since we are working with just the equatorial Kerr case, our results pertain to only two of these rays, one on each side. If these were the only two rays emanating from the source, we would see two point images on either side of the black hole. These are basically the antipodal points of the "ring" image that would be formed. We refer to these image positions as "para images"—"stardogs" or "parastars" are terms that would be appropriate as well. Angular positions for the para images are listed for the case when the source, lens and observer are perfectly aligned (i.e., $\beta = 0$). Table I is analogous to Table III in [19]. (The small discrepancies in the $\hat{a} = 0$ data compared to those obtained by [19] is due to rounding off in the physical constant and in conversion factors.) We use the weak deflection limit expansion for calculating θ_E for the stardog positions on the sky. The angular separation between the para, or stardog positions in the Kerr case is analogous to diameter of the Einstein ring in Schwarzschild geometry.

In the strong deflection limit, i.e., when the impact parameter is close to critical, we see multiple loops of the light ray as can be seen from the plot of the exact bending angle. Rays that loop around multiple times result in multiple relativistic para images on either

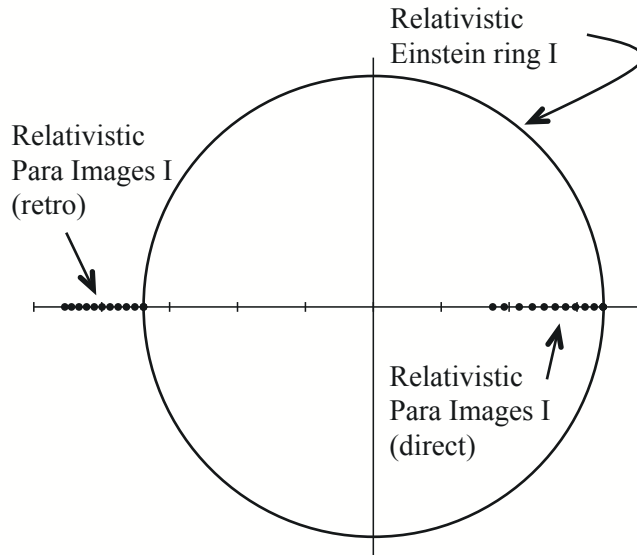


FIG. 5: Para positions or antipodal points on either side of the Kerr black hole where relativistic image I would appear on the sky, are shown as a function of increasing \hat{a} . The data used for this figure can be found in Table I.

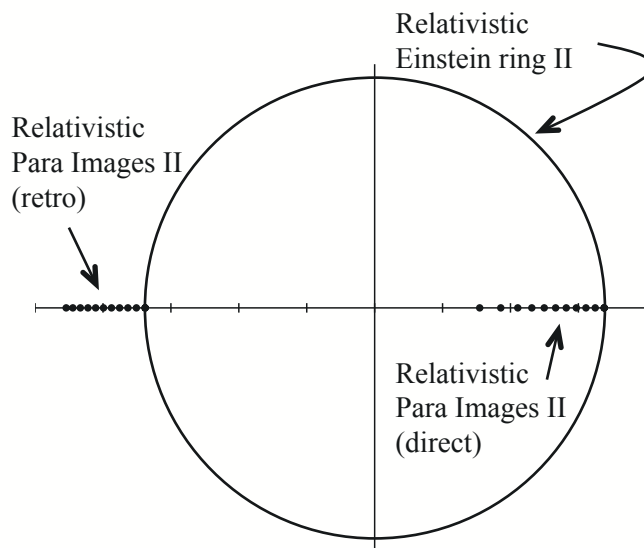


FIG. 6: Para positions or antipodal points on either side of the Kerr black hole where relativistic image I would appear on the sky, are shown as a function of increasing \hat{a} . The data used for this figure can be found in Table I.

Rings/Para images	a	θ	$\hat{\alpha}$	$r_0/2m_\bullet$	r_0/r_{crit}
Einstein ring	0	1.1583 arcsec	2.3166 arcsec	178074	
Para image:	(all spins)	1.1583 arcsec	2.3166 arcsec	178074	
Relativistic Einstein ring I	0	16.9207 μas	$2\pi + 33.8415 \mu\text{as}$	1.54505	1.03004
Relativistic Para image I:	0.000001	16.9203 μas	$2\pi + 33.8407 \mu\text{as}$	1.54462	1.02974
(direct)	0.1	16.2649 μas	$2\pi + 32.5299 \mu\text{as}$	1.48908	1.03330
	0.2	15.5890 μas	$2\pi + 31.1780 \mu\text{as}$	1.43143	1.03757
	0.3	14.8888 μas	$2\pi + 29.7776 \mu\text{as}$	1.37131	1.04281
	0.4	14.1595 μas	$2\pi + 28.3191 \mu\text{as}$	1.30821	1.04936
	0.5	13.3943 μas	$2\pi + 26.7885 \mu\text{as}$	1.24142	1.05774
	0.6	12.5829 μas	$2\pi + 25.1659 \mu\text{as}$	1.16982	1.06886
	0.7	11.7094 μas	$2\pi + 23.4187 \mu\text{as}$	1.09156	1.08433
	0.8	10.7447 μas	$2\pi + 21.4894 \mu\text{as}$	1.00335	1.10801
	0.9	9.6445 μas	$2\pi + 19.2891 \mu\text{as}$	0.90193	1.15792
	0.99	8.7941 μas	$2\pi + 17.5881 \mu\text{as}$	0.84449	1.44648
Relativistic Para image I:	0.000001	-16.9204 μas	$2\pi + 33.8407 \mu\text{as}$	1.54462	1.02974
(retro)	0.1	-17.5581 μas	$2\pi + 32.1162 \mu\text{as}$	1.59832	1.02675
	0.2	-18.1804 μas	$2\pi + 36.3608 \mu\text{as}$	1.65041	1.02420
	0.3	-18.7891 μas	$2\pi + 37.5783 \mu\text{as}$	1.70106	1.02201
	0.4	-19.3858 μas	$2\pi + 38.7716 \mu\text{as}$	1.75042	1.02011
	0.5	-19.9716 μas	$2\pi + 39.9432 \mu\text{as}$	1.79861	1.01844
	0.6	-20.5477 μas	$2\pi + 41.0953 \mu\text{as}$	1.84573	1.01697
	0.7	-21.1148 μas	$2\pi + 42.2296 \mu\text{as}$	1.89187	1.01567
	0.8	-21.6739 μas	$2\pi + 43.3477 \mu\text{as}$	1.93710	1.01452
	0.9	-22.2255 μas	$2\pi + 44.4510 \mu\text{as}$	1.98149	1.01348
	0.99	-22.7161 μas	$2\pi + 45.4321 \mu\text{as}$	2.02077	1.01264
Relativistic Einstein ring II	0	16.8996 μas	$4\pi + 33.7992 \mu\text{as}$	1.50188	1.00125
Relativistic Para image II:	0.000001	16.8996 μas	$4\pi + 33.7992\mu\text{as}$	1.50187	1.00125
(direct)	0.1	16.2393 μas	$4\pi + 32.4785\mu\text{as}$	1.44337	1.00158
	0.2	15.5568 μas	$4\pi + 31.1135 \mu\text{as}$	1.38239	1.00203
	0.3	14.8477 μas	$4\pi + 29.6954 \mu\text{as}$	1.31850	1.00265
	0.4	14.1060 μas	$4\pi + 28.2120 \mu\text{as}$	1.25112	1.00356
	0.5	13.3230 μas	$4\pi + 26.6460 \mu\text{as}$	1.17944	1.00494
	0.6	12.4853 μas	$4\pi + 24.9707 \mu\text{as}$	1.10226	1.00713
	0.7	11.5708 μas	$4\pi + 23.1417 \mu\text{as}$	1.01765	1.01091
	0.8	10.5376 μas	$4\pi + 21.0752 \mu\text{as}$	0.92208	1.01826
	0.9	9.2856 μas	$4\pi + 18.5713 \mu\text{as}$	0.80701	1.03606
	0.99	7.7345 μas	$4\pi + 15.4690 \mu\text{as}$	0.67348	1.15357
Relativistic Para image II:	0.000001	-16.8996 μas	$4\pi + 35.7992\mu\text{as}$	1.50188	1.00125
(retro)	0.1	-17.5411 μas	$4\pi + 35.0822 \mu\text{as}$	1.55824	1.00100
	0.2	-18.1664 μas	$4\pi + 36.3328 \mu\text{as}$	1.61272	1.00082
	0.3	-18.7774 μas	$4\pi + 37.5549 \mu\text{as}$	1.66554	1.00067
	0.4	-19.3760 μas	$4\pi + 38.7519 \mu\text{as}$	1.71688	1.00056
	0.5	-19.9633 μas	$4\pi + 39.9265 \mu\text{as}$	1.76687	1.00047
	0.6	-20.5405 μas	$4\pi + 41.0811 \mu\text{as}$	1.81564	1.00039
	0.7	-21.1087 μas	$4\pi + 42.2174 \mu\text{as}$	1.86329	1.00033
	0.8	-21.6686 μas	$4\pi + 43.3372 \mu\text{as}$	1.90992	1.00028
	0.9	-22.2209 μas	$4\pi + 44.4418 \mu\text{as}$	1.95561	1.00024
	0.99	-22.7120 μas	$4\pi + 45.4240 \mu\text{as}$	1.99598	1.00021

TABLE I: Para positions of Einstein and relativistic Einstein rings and the analogous images in Kerr geometry. Images on the retro side are indicated with negative values for the θ in microarcseconds (μas).

side just as in the Schwarzschild case. The image positions we obtain for direct orbits seem reasonable when compared with the higher order images studied by others for the non-zero spins for direct orbits off the equatorial plane (see Table I of [18] and [17] and references within.) We believe that image predictions for retro orbits for all spin values $0 \leq \hat{a} < 1$ have not appeared in literature before. Image positions for direct versus retro orbits illustrates the key difference in the effect the black hole spin has on rays that are traversing upstream versus downstream: the para images are pushed outward on the retro side and inward on the prograde side. The data used to generate Figures 5 and 6 are shown in Table I. Positive and negative values of the angular position θ of the image indicate respectively whether the image is on the right or left side. The last column in Table I gives the ratio r_0/r_{crit} , rather than $r_0/2m_\bullet$, showing clearly that the rays are just outside critical radii. We would like to reiterate here the importance of analytical expansion for the bending angle, without which calculation of these image positions would not be possible.

VII. CONCLUSIONS

Analytic solutions in the form of series expansions in the strong and weak deflection regimes for the bending angle of light rays on the equatorial plane of the Kerr black hole were presented in this paper. Higher order terms in strong deflection limit were not shown because they are too complicated. The technique to generate these, however, have been presented in detail. We have also shown that both expansions have a high level of accuracy compared to the exact bending angle, and so would be excellent predictors of image positions. To illustrate this, both expansions were applied to the simplest gravitational lensing situation when the source, lens and observer are perfectly aligned on the optic axis. We showed that the effect of the black hole spin distorts and shifts the Einstein ring inward on the direct side and outward on the retrograde side. For large spins, the shift in the image positions is much higher than the angular separation of successive relativistic images. Of course, whether this shift can be observed with precision will depend on the resolution power of future telescopes. The series expansions will be applied next to the case when the source is not on the optic axis and also calculations pertaining to magnification of the para images. In order to obtain the full geometric structure of images resulting from strong gravitational lensing, we plan to pursue a similar analysis of the full Kerr bending angle beyond the equatorial

plane. Our goal is to study the dependence of the bending angle on the inclination and the resulting variations in the image positions and magnifications in a perturbative framework that without any assumptions about the inclination angle or the black hole spin.

Acknowledgments

S. V. I. thanks Arlie O. Petters for numerous helpful discussions. E. C. H. was funded by the Dr. Jerry D. Reber Student/Faculty Research Fund at SUNY Geneseo. The authors thank Kevin Cassidy for his support of this research fund.

-
- [1] C. Darwin, Proc. R. Soc. London **A249**, 180 (1958); **A263**, 39 (1958).
 - [2] R. D. Atkinson, Astron. J. **70**, 517 (1965).
 - [3] J.-P. Luminet, Astron. Astrophys. **75**, 228 (1979).
 - [4] H. Ohanian, Am. J. Physics **55**, 428 (1987).
 - [5] S. Chandrasekhar, *The Mathematical Theory of Black Holes*, (Oxford, 1992).
 - [6] Misner, C., Thorne, K., & Wheeler, J., *Gravitation*, W. H. Freeman and Company, San Francisco (1973).
 - [7] S. V. Iyer and A. O. Petters, General Relativity and Gravitation **39**, 1563-1582 (2007).
 - [8] S. V. Iyer and E. C. Hansen, submitted for publication.
 - [9] K. Rauch and R. Blandford, ApJ, **421**, 46 (1994).
 - [10] R. H. Boyer, R. W. Lindquist, J. Math. Phys, **8**, (No. 2), 265 (1967).
 - [11] G. V. Skroetskii, Dokl. Akad. Nauk SSR **114**, 73 (1957) [English trans.:Soviet Phys.–Doklady **2**, 226 (1957)].
 - [12] J. Plebanski, Phys. Rev. **118**, 1396 (1960).
 - [13] Private communication
 - [14] I. Bray, Phys Rev. D **34**, 367, (1986).
 - [15] L. J. Goicoechea, E. Mediavilla, J. Buitrago and F. Atrio, Mon. Not. R. Astron. Sco. **259**, 281, (1992).
 - [16] J. F. Glicenstein, Astron. Astrophys. **343**, 1025, (1999).

- [17] V. Bozza and G. Scarpetta, Phys. Rev. D. **76**, 083008 (2007). V. Bozza, Nuovo Cim. **122B** 547-556, (2007). See references here for a complete list of work of Bozza et al.
- [18] S. E. Vazquez and E. P. Esteban, Nuovo Cim. **119B** 489-519, (2004).
- [19] K. S. Virbhadra and G. F. R. Ellis, Phys. Rev. D **62**, 084003 (2000).
- [20] see for example, <http://functions.wolfram.com> (Wolfram Mathematica web site)

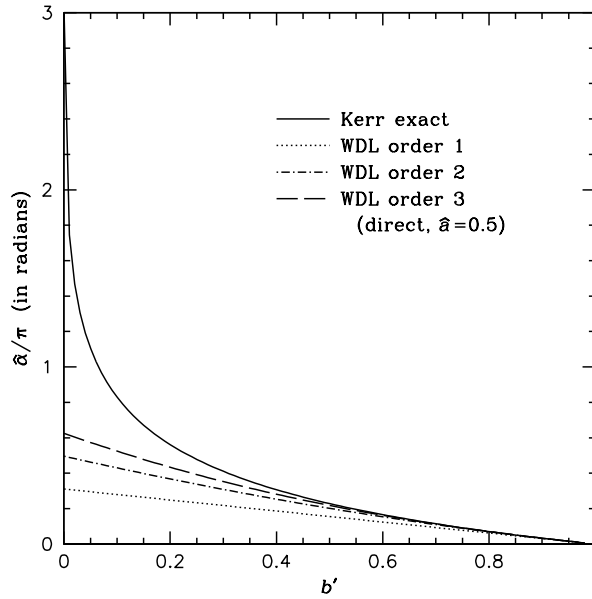


FIG. 7: Plot comparison of perturbative and exact angle for $\hat{a} = 0.5$ direct orbit.

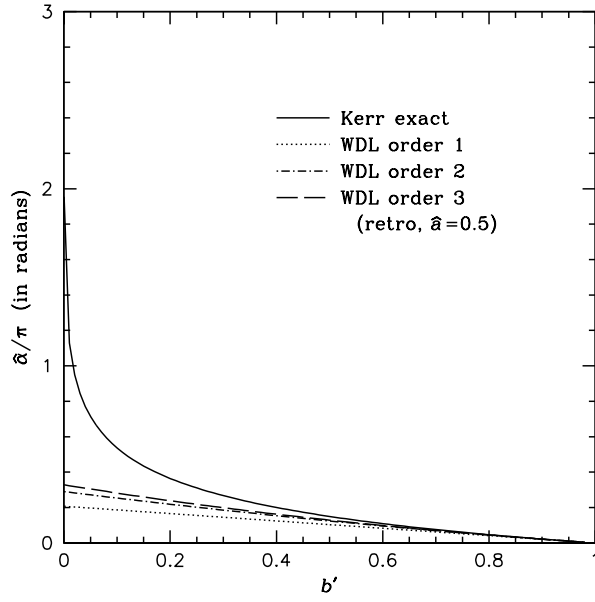


FIG. 8: Plot comparison of perturbative and exact angle for $\hat{a} = 0.5$ retro orbit.

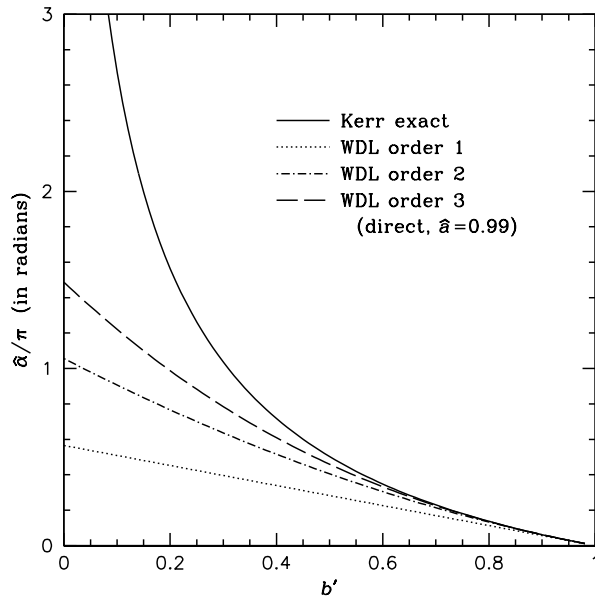


FIG. 9: Plot comparison of perturbative and exact angle for $\hat{a} = 0.99$ direct orbit.

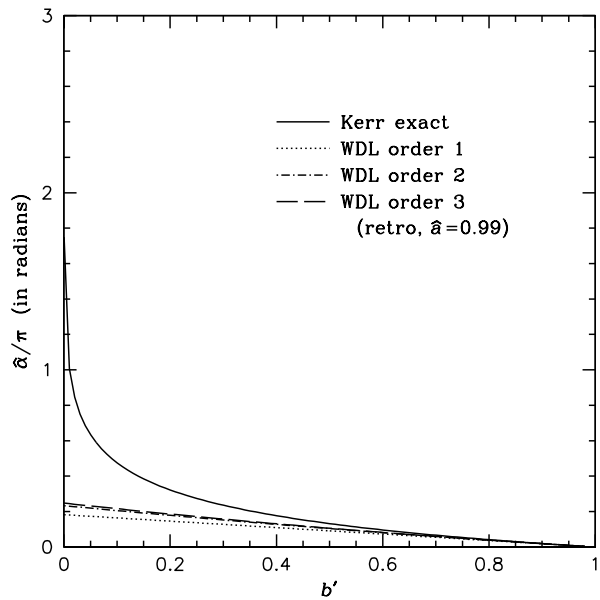


FIG. 10: Plot comparison of perturbative and exact angle for $\hat{a} = 0.99$ retro orbit.

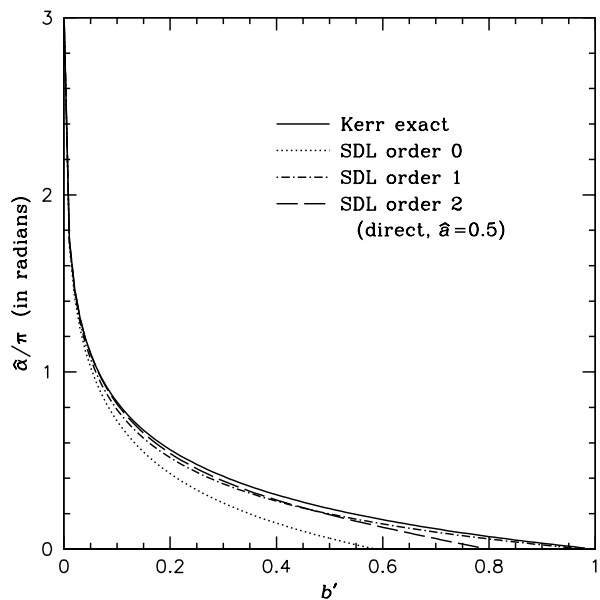


FIG. 11: Plot comparison of perturbative and exact angle for $\hat{a} = 0.5$ direct orbit.

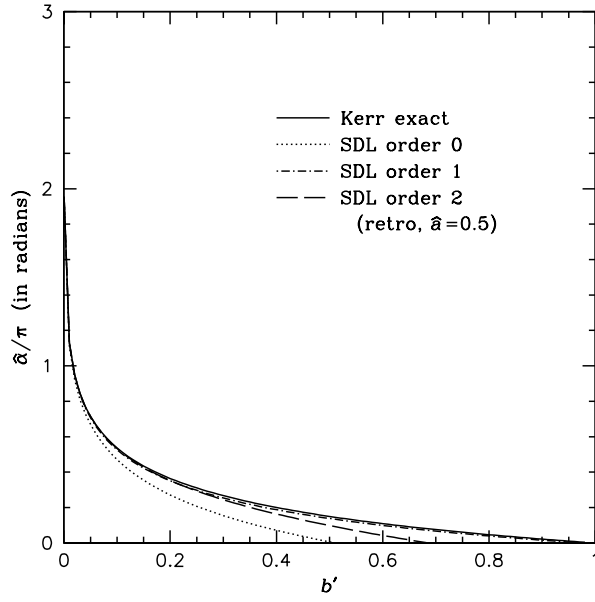


FIG. 12: Plot comparison of perturbative and exact angle for $\hat{a} = 0.5$ retro orbit.

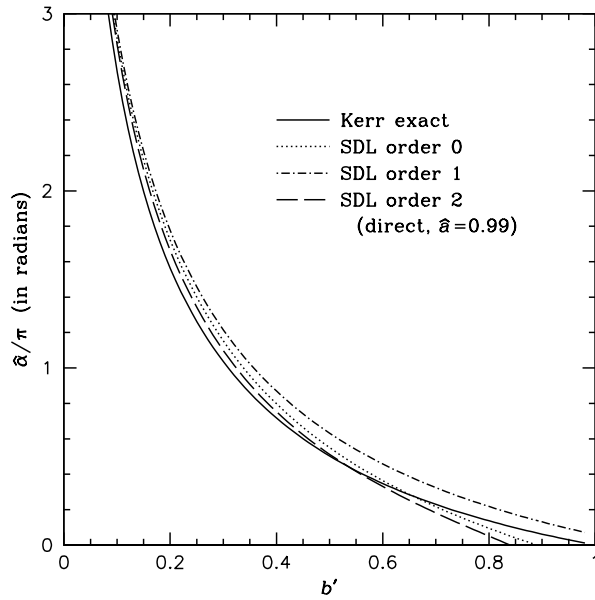


FIG. 13: Plot comparison of perturbative and exact angle for $\hat{a} = 0.99$ direct orbit.

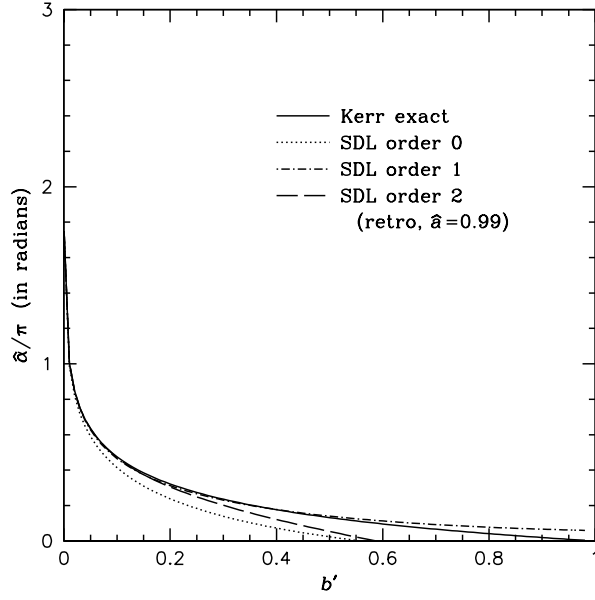


FIG. 14: Plot comparison of perturbative and exact angle for $\hat{a} = 0.99$ retro orbit.

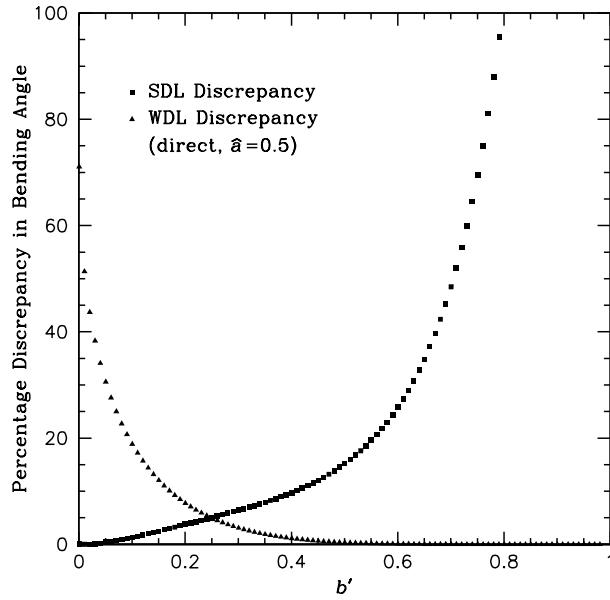


FIG. 15: Percentage discrepancy for 2nd-order strong deflection and the 6th-order weak deflection for direct orbit with $\hat{a} = 0.5$. The horizontal axis corresponds to the exact value.

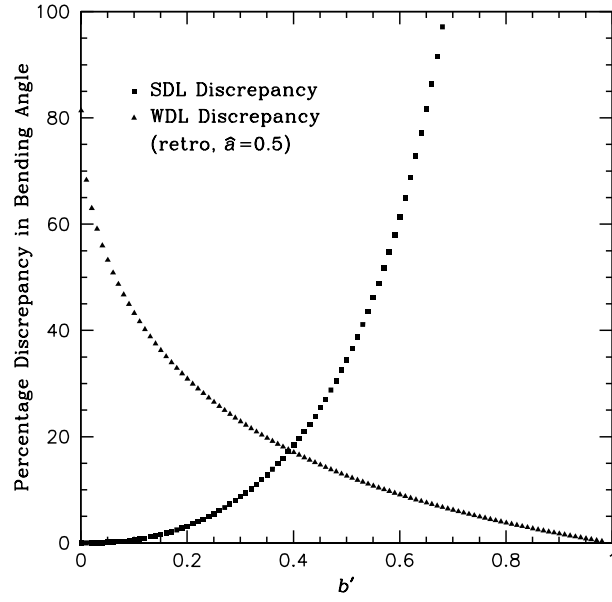


FIG. 16: Percentage discrepancy for 2nd-order strong deflection and the 6th-order weak deflection for retro orbit with $\hat{a} = 0.5$. The horizontal axis corresponds to the exact value.